Structural and magnetic phase diagrams of $La_{1-x}Sr_xMnO_3$ and $Pr_{1-y}Sr_yMnO_3$

O. Chmaissem,[1,2] B. Dabrowski,[1,2] S. Kolesnik,[1] J. Mais,[1] J. D. Jorgensen,[2] and S. Short[2]
[1]*Department of Physics, Northern Illinois University, DeKalb, Illinois 60115*
[2]*Materials Science Division, Argonne National Laboratory, Argonne, Illinois 60439*
(Received 30 September 2002; revised manuscript received 16 January 2003; published 31 March 2003)

The nuclear and magnetic structures and properties of $La_{1-x}Sr_xMnO_3$ with $0.45 \leqslant x \leqslant 1$ and $Pr_{1-y}Sr_yMnO_3$ ($0.58 \leqslant y \leqslant 1$) were investigated using neutron powder diffraction, resistivity and magnetic measurements. In this paper, we present the full magnetic and structural phase diagram for $La_{1-x}Sr_xMnO_3$ and a partial phase diagram for $Pr_{1-y}Sr_yMnO_3$. At low temperatures, we observe a series of structural phase transitions evolving as a function of increasing x as follows: orthorhombic $Pbnm \rightarrow$ rhombohedral $R\bar{3}c \rightarrow$ orthorhombic $Fmmm$ $\rightarrow$ tetragonal $I4/mcm \rightarrow$ cubic $Pm\bar{3}m$. At higher temperatures, the orthorhombic *Fmmm* structural region disappears. We also identify four magnetic states (*FM*, *A*, *C*, and *G* type) evolving as a function of increasing x. The magnetic and nuclear structural transitions coincide for samples with $0.8 \leqslant x \leqslant 0.95$. In the $0.5 \leqslant x \leqslant 0.9$ region, resistivity and magnetic measurements show a substantial hysteresis near T_N. This hysteresis of a few K is indicative of a first order antiferromagnetic transition in good agreement with the neutron diffraction results. Our data also suggest the existence of a strong competition between the ferromagnetic and *A*-type states for $x \sim 0.5$, and between the *C*- and *G*-type states for $x \sim 0.95$. A similar behavior is observed for $Pr_{1-y}Sr_yMnO_3$.

DOI: 10.1103/PhysRevB.67.094431 PACS number(s): 75.25.+z, 75.30.−m, 61.12.−q, 81.05.−t

INTRODUCTION

Extensive studies probing the properties of $R_{1-x}A_xMnO_3$ (R=La, Pr, Nd, etc.; A=Sr, Ca) resulted in the demonstration of exciting physical and structural properties that are very sensitive to subtle structural distortions or to small changes in the hole or electron concentration at the Mn sites (e.g., varying the carrier density in these materials could lead to insulating, metallic ferromagnetic (FM), or *A*-, *C*-, *CE*-, or *G*-type antiferromagnetic (AFM) properties and for certain compositions to charge and/or orbital ordering of the Mn^{3+} and Mn^{4+} ions). Using first-principles band structure calculations based on the generalized gradient approximation, Fang and his co-workers[1] modeled the magnetic properties of a highly substituted system, namely, $Sm_{1-x}Ca_xMnO_3$, in terms of a relationship between the magnitude of the c/a ratio and the stability of the magnetic state of the material. Indeed, the calculations of Fang *et al.*'s were supported by the observation of *C*- and *G*-type[2,3] antiferromagnetic states in $Sm_{1-x}Ca_xMnO_3$ for $x \sim 0.8$ and $0.85 \leqslant x \leqslant 1$, respectively, and by the experimental results of Konishi and co-workers[4] showing that the c/a ratios and the magnetic states of $La_{1-x}Sr_xMnO_3$ thin films can be controlled by using substrates of different lattice mismatch. On the other hand, van der Brink and Khomskii[5] proposed that the stability of the FM state and the *A*- and *C*-type AFM states is due to a double exchange mechanism via degenerate e_g orbitals.

The structures and properties of $R_{1-x}Sr_xMnO_3$ samples with low strontium content ($x < 0.5$) are well known.[6–9] On the other hand, the properties of samples with higher Sr contents, which are difficult to synthesize under normal conditions, are less understood.[10–15] For example, both metallic and nonmetallic *A*-type antiferromagnetic $La_{1-x}(Pr_{1-x})Sr_xMnO_3$ samples were reported.[13,16–19] $Pr_{0.5}Sr_{0.5}MnO_3$ was reported to have an orthorhombic *Pbnm*,[20] tetragonal $F4/mmc$,[21] or tetragonal $I4/mcm$ (Ref. 12) structure at room temperature, and a monoclinic $P2_I/n$ (Refs. 22, 23) or orthorhombic *Fmmm* (Ref. 12) structure at low temperatures. $La_{1-x}Sr_xMnO_3$ samples with $0.5 \leqslant x \leqslant 1$, on the other hand, were reported to be either cubic[12] at room temperature or not single phase.[13] Clearly, reliable data are lacking because of the inherent difficulty in synthesizing high quality samples in this composition range. It is, therefore, important to determine the complete composition phase diagram for the $La_{1-x}Sr_xMnO_3$ and $Pr_{1-y}Sr_yMnO_3$ systems that present small structural distortions at high Sr substitution levels (almost straight Mn-O-Mn bond angles) and compare their properties to other systems, for example, $R_{1-x}Ca_xMnO_3$ with large structural distortions. In this paper, we present a detailed study of the structural and physical properties of $La_{1-x}Sr_xMnO_3$ and $Pr_{1-y}Sr_yMnO_3$ in the composition range of $0.45 \leqslant x(y) \leqslant 1$ with special attention being paid to samples near the phase boundaries that separate different magnetically ordered states.

EXPERIMENTAL DETAILS

$R_{1-x}Ca_xMnO_3$ with $0 \leqslant x \leqslant 1$ and $R_{1-x}Sr_xMnO_3$ with $x < 0.5$ can be easily synthesized under normal conditions in the perovskite structure. However, perovskite samples with higher Sr content—of larger ionic size—are much more difficult to stabilize because of the decreasing average size of the Mn^{3+x} ions and the unfavorable tolerance factor of the desired final phase. Normal synthesis conditions usually yield samples that contain a second hexagonal phase of $SrMnO_3$ crystallizing in the $P6_3/mmc$ structure. For this work, polycrystalline $La_{1-x}Sr_xMnO_3$ and $Pr_{1-y}Sr_yMnO_3$ ($0.45 \leqslant x \leqslant 1$ and $0.58 \leqslant y \leqslant 1$) perovskite samples were synthesized from stoichiometric mixtures of prefired La_2O_3, Pr_4O_7, $SrCO_3$, and MnO_2 using a two-step method previously developed for similar metastable compounds.[24] In a

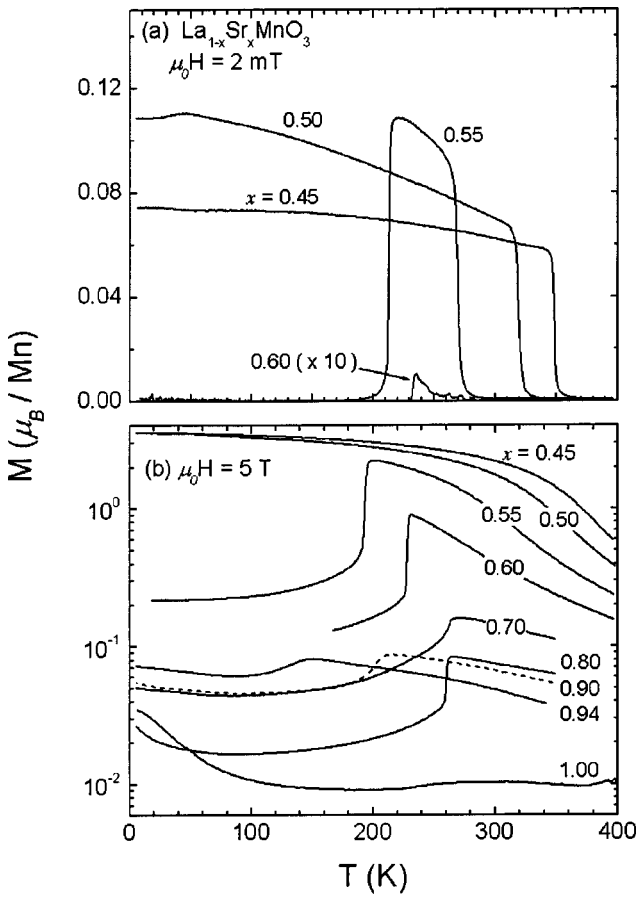

FIG. 1. (a) Low field magnetization (2 mT) measurements of $La_{1-x}Sr_xMnO_3$. (b) "Field-cooled (FC)" magnetization measurements at 5 T.

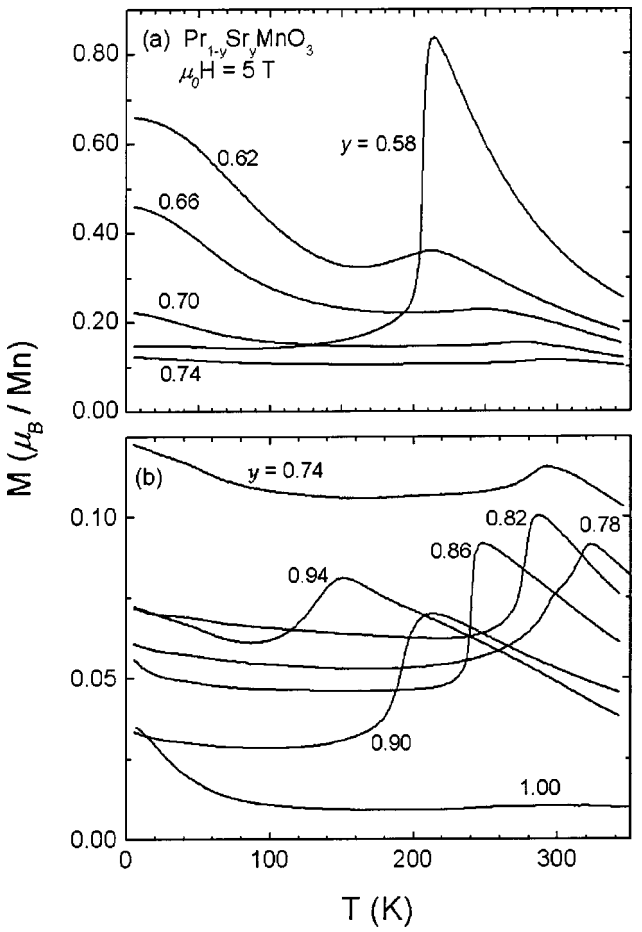

FIG. 2. Field-cooled magnetization measurements of $Pr_{1-y}Sr_yMnO_3$ at 5 T. For this series with $y \geqslant 0.58$, no significant ferromagnetic signal was observed at 2 mT.

first step, single-phase oxygen-deficient perovskites are obtained from precursors fired in flowing argon gas (containing ~10 ppm O_2 or less) at temperatures up to 1400 °C for $x = 1$ ($SrMnO_{2.61}$). In the second step, the oxygen-deficient samples were annealed in air at 500 °C followed by slow cooling to room temperature to bring the oxygen content up to 3.00 ± 0.01 oxygen atoms per formula unit (stoichiometry was carefully monitored using thermogravimetric analysis). All samples were found to be single-phase from x-ray and neutron powder diffraction data.

The magnetic and resistive properties of the samples were determined from measurements performed using a Quantum Design Physical Properties Measurement System-Model 6000 at temperatures between 10 and 350 K. Time-of-flight neutron powder diffraction data were collected on the Special Environment Powder Diffractometer (SEPD)[25] at the Intense Pulsed Neutron Source (IPNS). Diffraction data for $x = 0.45$, 0.5, 0.55, 0.6, 0.8, 0.9, 0.94, 1.0 and $y = 0.58$, 0.66, 0.74, 0.78, 0.86, 0.90, 0.94 were acquired as a function of temperature using a closed-cycle helium refrigerator with heating capabilities. Data for an $x = 0.7$ sample were collected at room temperature. High-resolution backscattering data, from 0.5 to 4 Å, were analyzed using the Rietveld method and the General Structure Analysis System (GSAS) code.[26] For $x = 0.9$ and 0.94, forward-scattering data up to 10 Å were also used in the refinements because they contain magnetic peaks of the *C* and *G* type of considerable intensities. In the analysis, background, peak width, and the extinction parameter were refined, together with the lattice parameters, atom positions, and isotropic and anisotropic temperature factors for the cations and oxygen atoms, respectively.

RESULTS AND DISCUSSION

Magnetic and resistivity measurements. Ferromagnetic properties were observed in the low field magnetization measurements ($\mu_0 H = 2$ mT) of $La_{1-x}Sr_xMnO_3$ only for the $x = 0.45$, 0.5 samples below $T_c = 348$ and 330 K, respectively, and for the $x = 0.55$ sample over a temperature range of ~212–270 K, Fig. 1(a). At 5 T, measurements of the temperature dependence of "field-cooled" (FC) magnetization, displayed on a logarithmic scale in Fig. 1(b), show a saturation value of $\sim 3.5 \mu_B$ for the $x = 0.45$ and 0.5 samples. A sharp drop in magnetization is observed for the $x = 0.55$ and 0.6 samples below a Néel temperature (T_N) of ~195 and 230 K, respectively (defined as the temperature at which the drop in magnetization corresponds to the transition from a ferromagnetic or paramagnetic state to an antiferromagnetic

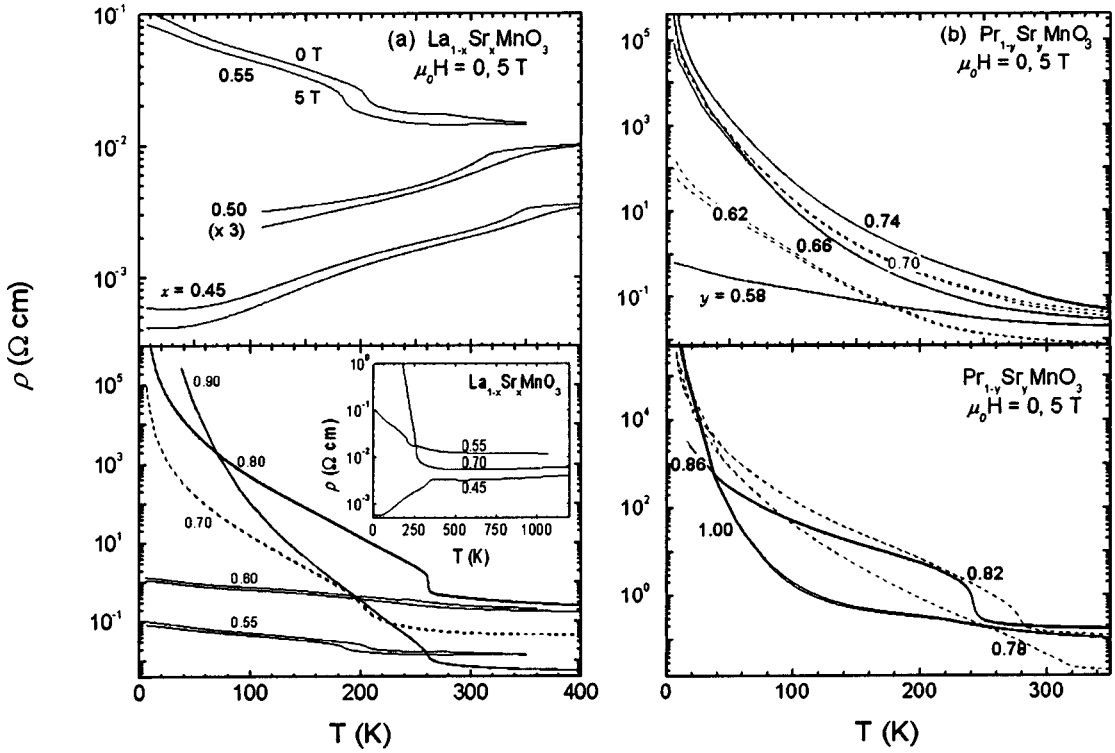

FIG. 3. Resistivity measurements at 0 and 5 T of $La_{1-x}Sr_xMnO_3$ (a) and $Pr_{1-y}Sr_yMnO_3$ (b). High-temperature resistivity measurements for $x=0.45$, 0.55, and 0.7 are shown in the inset.

state). For the $x=0.55$ sample, the application of a 5 T magnetic field results in a considerable decrease of T_N from 212 to 195 K and an increase of T_C from 270 to ~320 K. The $0.7 \leqslant x \leqslant 0.95$ samples remain antiferromagnetic at 5 T, with only a very small ferromagnetic component observed near T_N. No significant ferromagnetic component is observed for $SrMnO_3$ ($x=1.0$) as expected from its regular ''undistorted'' structure that remains cubic at all temperatures.

For the $Pr_{1-y}Sr_yMnO_3$ samples, similar behavior is observed for the $y=0.58$ and $0.74<y\leqslant 0.94$ samples showing a drop in magnetization at the onset of the AFM ordering, Fig. 2(a). Magnetization measurements of the remaining samples show AFM transitions over a somewhat broader temperature range and a small but measurable FM component remains present at low temperatures, Fig. 2(b).

Measurements at 0 and 5 T of the resistivity of $La_{1-x}Sr_xMnO_3$ and $Pr_{1-y}Sr_yMnO_3$ show a semimetallic character in the paramagnetic state and an insulating behavior below T_N for all antiferromagnetic samples except the $x=0.5$ sample, Fig. 3. As shown in the figure, the $x=0.5$ sample—containing both FM and AFM phases below T_N in zero field as discussed in the next section—and the ferromagnetic $x=0.45$ sample are the only samples that show a metallic behavior at low temperatures. The $x=0.55$ sample shows a metallic behavior between 210 and 280 K and ~190 and 320 K in 0 and 5 T, respectively, i.e., over a temperature range corresponding to the ferromagnetic phase at these fields. Finally, it is important to note the increase in the magnitude of the resistivity at 5 K from $\sim 4\times 10^{-4}$ to $>10^6$ Ω cm as a function of increasing x (or y). This behavior can be explained by the progressive change of the magnetic state of the samples from FM to *A*-, *C*-, and *G*-type AFM as a function of increasing x (or y) as will be discussed in the next section. Resistivity measurements at temperatures up to 1200 K, displayed in the inset of Fig. 3, for three representative samples ($x=0.45$, 0.55, and 0.7) show a metallic behavior at high temperatures. T_C and T_N values extracted from the magnetic and resistive measurements will be used throughout this paper when referring to the magnetic properties of our samples.

Both magnetization and resistivity measurements carried out as a function of increasing and decreasing temperature show a substantial hysteresis near T_N for $0.5\leqslant x\leqslant 0.9$, $y=0.58$, and $0.78<y<0.9$ as displayed in Fig. 4. The hysteresis of a few K is indicative of a first-order antiferromagnetic transition, in good agreement with the neutron diffraction results.

Neutron powder diffraction. Extensive studies have been previously performed in the narrow composition range of $0\leqslant x\leqslant 0.2$ and to a lesser extent in the $0.2\leqslant x\leqslant 0.5$ range.[6–9] These studies resulted in a well established partial phase diagram $La_{1-x}Sr_xMnO_3$ and in a good understanding of the structural and physical properties as a function of x and synthesis conditions in this limited composition range. For example, different synthesis conditions for $LaMnO_{3-\delta}$ result in four different crystallographic phases: AFM orthorhombic and FM orthorhombic, monoclinic, or rhombohedral.[27] In a previous study,[6] we showed that these structures are related to the oxygen soichiometry/non-stoichiometry of the samples and that stoichiometric samples exhibit an AFM structure with a large Jahn-Teller distortion and a T_N of ~140 K for $\delta=0$. In the $0.1\leqslant x\leqslant 0.2$ range,[6] the Curie temperature (T_C)

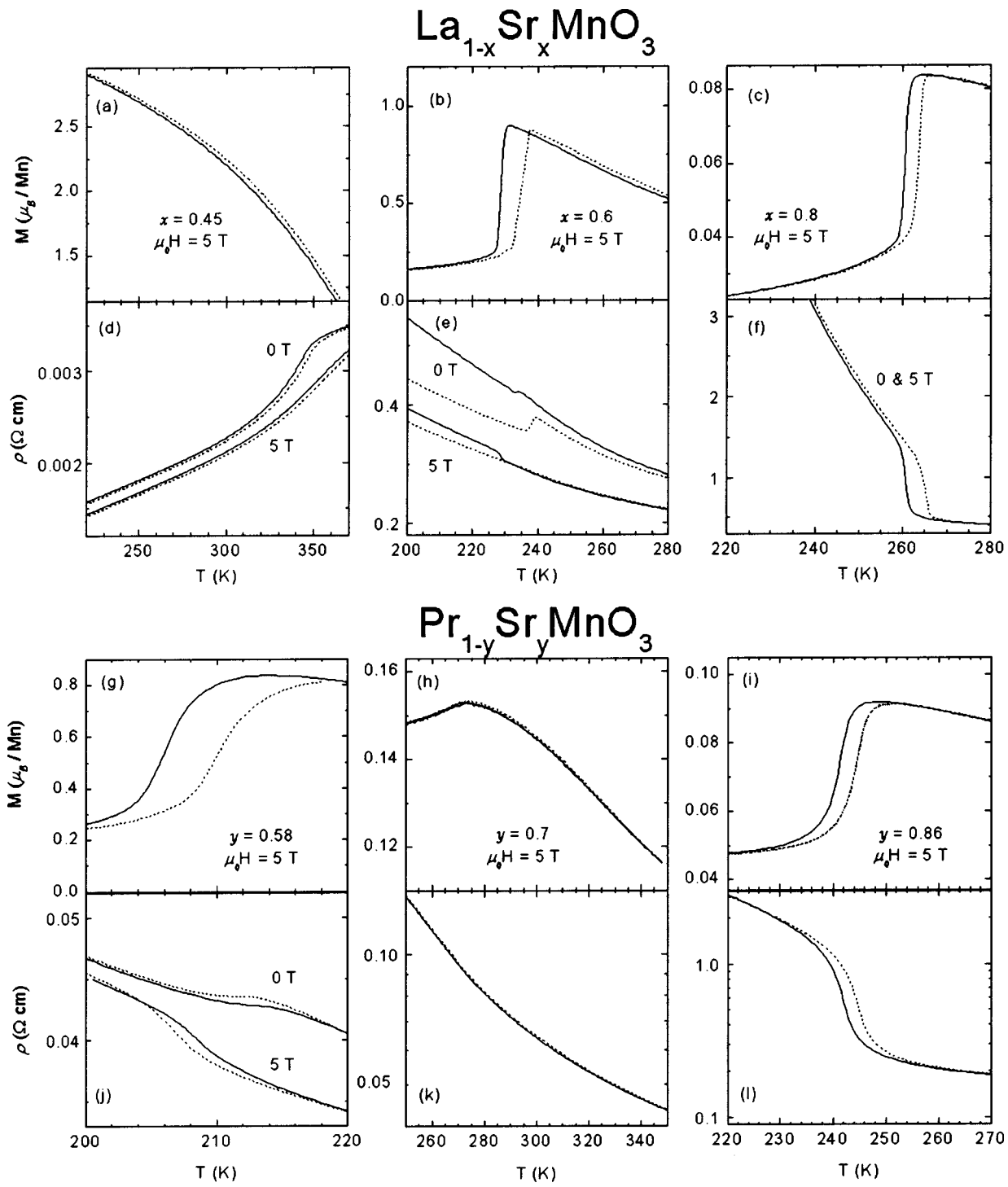

FIG. 4. Zero-field cooled (dashed lines) and field cooled (solid lines) magnetization (a)–(c); (g)–(i) and resistivity (d)–(f), (j)–(l) data for $La_{1-x}Sr_xMnO_3$ and $Pr_{1-y}Sr_yMnO_3$. For some samples, a substantial hysteresis is observed near T_N indicative of a first-order phase transition (see text for more details).

increases linearly with increasing Sr content while the temperature of an orbital ordering transition to a state with a large coherent Jahn-Teller (JT) distortion decreases. These two phase transition lines cross at $x=0.145$ and $T=210$ K. In this limited phase diagram, several regions are identified in which the samples exhibit large or small coherent and incoherent JT distortions. For Sr contents higher than ~ 0.16, the rhombohedral structure is energetically more stable than other structures and remains so up to $x\sim 0.45$. No structural competition has ever been observed in the composition range $0.16 \leqslant x \leqslant 0.45$. Neutron diffraction patterns of $La_{0.55}Sr_{0.45}MnO_3$, displayed in Fig. 5, show that this phase remains rhombohedral at all measured temperatures between 30 and 550 K.

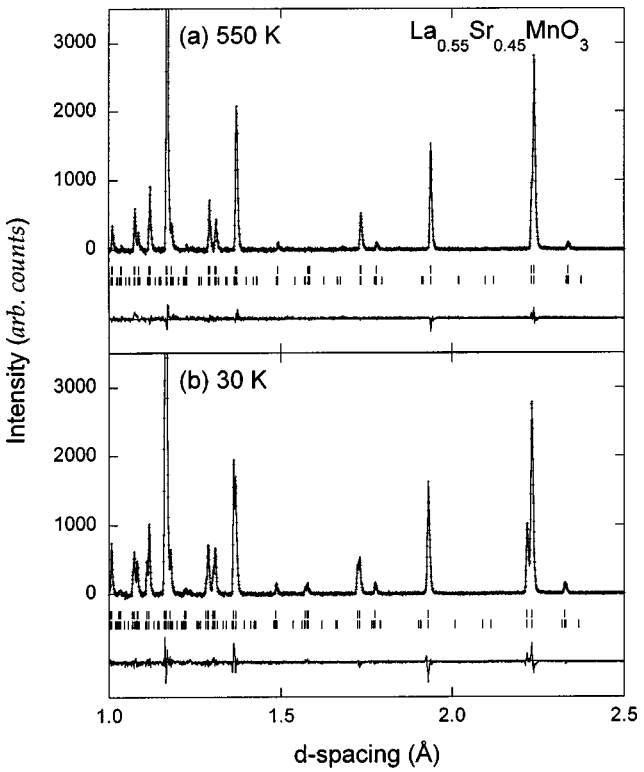

FIG. 5. Neutron powder diffraction data and best-fit Rietveld refinements of $La_{0.55}Sr_{0.45}MnO_3$ at 30 and 550 K showing rhombohedral $R\bar{3}c$ patterns. Tick marks shown under the patterns indicate the positions of the nuclear and magnetic Bragg peaks.

Phase diagrams. In the composition range $0.5 \leqslant x(y) \leqslant 1$, $La_{1-x}Sr_xMnO_3$ and $Pr_{1-y}Sr_yMnO_3$ systems exhibit similar structural and magnetic properties. In Fig. 6, we plot the full phase diagram of $La_{1-x}Sr_xMnO_3$ and a partial phase diagram of $Pr_{1-y}Sr_yMnO_3$ with $0.5 \leqslant y \leqslant 1$ in which we identify three structural regions: cubic $Pm\bar{3}m$, tetragonal $I4/mcm$, and orthorhombic *Fmmm* that are functions of temperature and composition. These phase diagrams were constructed by studying several well selected compositions of $La_{1-x}Sr_xMnO_3$ and $Pr_{1-y}Sr_yMnO_3$ as a function of temperature. This study included the Rietveld refinement of backscattering and 90° data sets. Details of the data for some individual compositions will be given later. First, however, the general features of the phase diagrams will be described. Data for the $La_{1-x}Sr_xMnO_3$ phase diagram with $0 \leqslant x \leqslant 0.45$ were extracted from our previously published work.[6,28]

The highly doped end member of both phase diagrams $SrMnO_3$ ($x=y=1$) crystallizes in a simple cubic $Pm\bar{3}m$ structure in which undistorted corner-sharing MnO_6 octahedra are stacked three dimensionally and the $(La\ or\ Pr)_{1-x}Sr_x$ ions occupy the space between the octahedra. This cubic structure extends to lower values of x in both systems, as shown in Fig. 6, with a transformation to a tetragonal phase around $x=0.7$ at room temperature and increasingly higher values of x at lower temperature. The tetragonal $I4/mcm$ structure is the result of elongation and rotation of the MnO_6 octahedra along and around the c axis, respectively, resulting

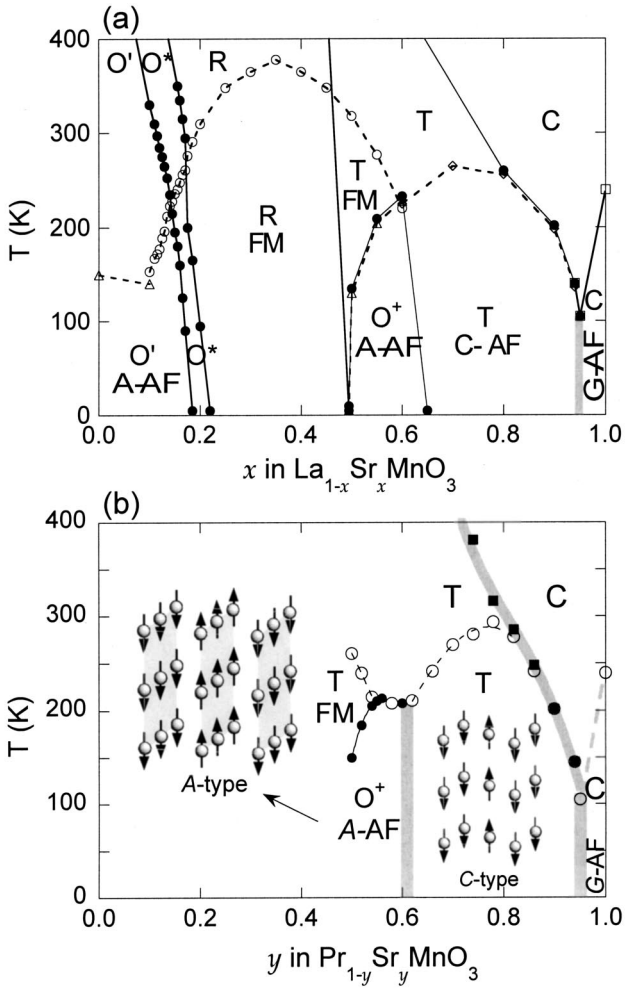

FIG. 6. Magnetic and structural phase diagrams for $La_{1-x}Sr_xMnO_3$ (a) and $Pr_{1-y}Sr_yMnO_3$ (b). *A*- and *C*-type AFM structures are shown in (b). Structural and magnetic transition boundaries are shown as solid and dashed lines, respectively. The symbols *C*, *T*, *R*, and *O* refer to cubic, tetragonal, rhombohedral, and orthorhombic symmetries, respectively. Coherent and incoherent Jahn-Teller distortions are present in the *O′* and *O** *Pbnm* structures, respectively. O^+ refers to a *Fmmm* orthorhombic symmetry (see text and Table I for more details).

in two equivalent apical oxygen atoms, O(1), and four equivalent in-plane oxygen atoms, O(2), with one unique rotation angle of the Mn octahedron around the c axis. Upon decreasing temperature in the approximate composition range 0.5–0.6, the tetragonal structure transforms to an orthorhombic structure. In the low-temperature orthorhombic *Fmmm* structure, the Mn ions are bonded with two independent in-plane pairs of oxygen atoms, O(2) and O(3), that rotate independently around the c axis, thus, making two angles that are only slightly different from each other. The structural parameters of several representative samples with different structures for the $La_{1-x}Sr_xMnO_3$ series are listed in Table I. The evolution of the room temperature reduced unit cell volume of the full $La_{1-x}Sr_xMnO_3$ series is presented in Fig. 7(a) as a function of x. The figure shows a linear relationship between the two parameters for $0.2 < x < 1$ despite

TABLE I. Structural parameters of selected $La_{1-x}Sr_xMnO_3$ samples.

x	0.45	0.5	0.5	0.55	0.55	0.6	0.6	0.7	0.8	0.9	1.0
T (K)	300 K	310 K	38 K	290 K	12 K	300 K	50 K	300 K	300 K	300 K	290 K
	$R\bar{3}c$	$I4/mcm$	$Fmmm$	$I4/mcm$	$Fmmm$	$I4/mcm$	$Fmmm$	$I4/mcm$	$Pm\bar{3}m$	$Pm\bar{3}m$	$Pm\bar{3}m$
a (Å)	5.47598(4)	5.44461(5)	7.5654(3)	5.43378(4)	7.5600(1)	5.42964(4)	7.55665(4)	5.43018(8)	3.82549(2)	3.81811(3)	3.8041(3)
b (Å)	5.47598(4)		7.7531(2)		7.7300(2)		7.72087(4)				
c (Å)	13.3461(1)	7.7595(1)	7.7885(2)	7.7455(1)	7.7833(2)	7.7381(1)	7.77595(4)	7.6704(2)			
γ (°)	120										
V (Å^3)	346.583(5)	230.021(5)	456.83(3)	228.694(4)	454.85(1)	228.127(4)	453.679(7)	226.176(3)	55.984(1)	55.660(1)	55.04875(1)
x (La, Sr)	0	0.5	0	0.5	0	0.5	0	0.5	0.5	0.5	0.5
y (La, Sr)	0	0	0	0	0	0	0	0	0.5	0.5	0.5
z (La, Sr)	0.25	0.25	0.2499(4)	0.25	0.2510(3)	0.25	0.2505(2)	0.25	0.5	0.5	0.5
U_{iso} (La, Sr)	0.60(3)	0.57(3)	0.16(6)	0.52(2)	0.03(3)	0.60(2)	0.17(2)	0.58(1)	0.57(2)	0.55(3)	0.60(3)
x (Mn)	0	0	0.25	0	0.25	0	0.25	0	0	0	0
y (Mn)	0	0	0.25	0	0.25	0	0.25	0	0	0	0
z (Mn)	0	0	0	0	0	0	0	0	0	0	0
U_{iso} (Mn)	0.26(3)	0.27(3)	−0.11(7)	0.22(2)	−0.006(33)	0.21(3)	−0.02(3)	0.24(2)	0.25(2)	0.26(4)	0.28(2)
M (μ_B)	1.47(5)		2.60(5)		2.82(2)		2.48(2)				
x (O1)	0.4702(1)	0	0.25	0	0.25	0	0.25	0	0	0	0
y (O1)	0	0	0.25	0	0.25	0	0.25	0	0	0	0
z (O1)	0.25	0.25	0.25	0.25	0.25	0.25	0.25	0.25	0.5	0.5	0.5
U_{11} (O1)	1.08(3)	1.35(7)	1.4(2)	1.29(5)	0.9(1)	1.04(6)	0.44(7)	1.1(3)	0.89(2)	0.91(4)	0.87(3)
U_{22} (O1)	0.85(6)	1.35(7)	1.0(2)	1.29(5)	0.33(8)	1.04(6)	0.56(7)	1.1(3)	0.89(2)	0.91(4)	0.87(3)
U_{33} (O1)	1.02(4)	0.6(1)	0.1(2)	0.44(9)	0.21(9)	0.61(9)	0.31(7)	0.4(2)	0.41(4)	0.34(7)	0.37(5)
U_{12} (O1)	0.42(3)										
U_{13} (O1)	−0.23(2)										
U_{23} (O1)	−0.46(5)										
x (O2)		0.2720(2)	0.2259(6)	0.2700(1)	0.2273(3)	0.2665(2)	0.2291(3)	0.2519(5)			
y (O2)		0.7720(2)	0	0.7700(1)	0	0.7665(2)	0	0.7519(5)			
z (O2)		0	0	0	0	0	0	0			
U_{11} (O2)		0.78(3)	−0.2(1)	0.83(3)	0.04(8)	0.77(3)	0.16(7)	0.8(1)			
U_{22} (O2)		0.78(3)	0.3(2)	0.83(3)	0.09(9)	0.77(3)	0.23(7)	0.8(1)			
U_{33} (O2)		1.14(7)	1.6(3)	0.80(6)	0.5(1)	1.10(6)	0.51(10)	0.9(1)			
U_{12} (O2)		0.25(5)		0.29(4)		0.41(5)		0.4(2)			
x (O3)			0		0		0				
y (O3)			0.2790(4)		0.2737(3)		0.2711(2)				
z (O3)			0		0		0				
U_{11} (O3)			0.2(1)		0.33(7)		0.15(6)				
U_{22} (O3)			−0.7(1)		0.00(8)		0.47(7)				
U_{33} (O3)			0.4(2)		0.5(1)		0.41(10)				
R_p (%)	5.13	6.01	6.57	4.01	4.86	6.1	6.01	4.73	6.48	7.21	5.65
R_{wp} (%)	8.37	9.35	9.87	5.96	7.28	10.01	9.84	6.88	10.13	11.18	8.75
R_{nucl} (%)	4.87	4.70	2.76	4.13	2.41	4.88	2.93	5.18	5.59	6.37	5.08
R_{mag} (%)	15.20		12.15		10.53		9.16				
χ^2	1.282	1.604	1.847	1.639	2.469	1.324	1.286	1.98	1.423	1.182	1.544

the various phase transitions that occur with increasing x. In the range $0<x<0.2$, large Jahn-Teller distortions result in smooth but nonlinear effects on the behavior of the unit cell volume with respect to x.

The evolution of the (La, Sr)-O (Pr, Sr)-O and Mn-O bond lengths as a function of x or y is shown in Fig. 7(b). Refined values (open symbols) as well as algebraic and geometric[29] averages (closed symbols) are shown on the figure. Solid lines through the average bonds are a guide to the eye. Once again, the relationship between the average bond lengths and x is linear for most of the compositions except for those where the Jahn-Teller effect is dominant. As shown in the figure, the behavior and magnitude of the average Mn-O bonds extracted from the La/Sr and Pr/Sr series

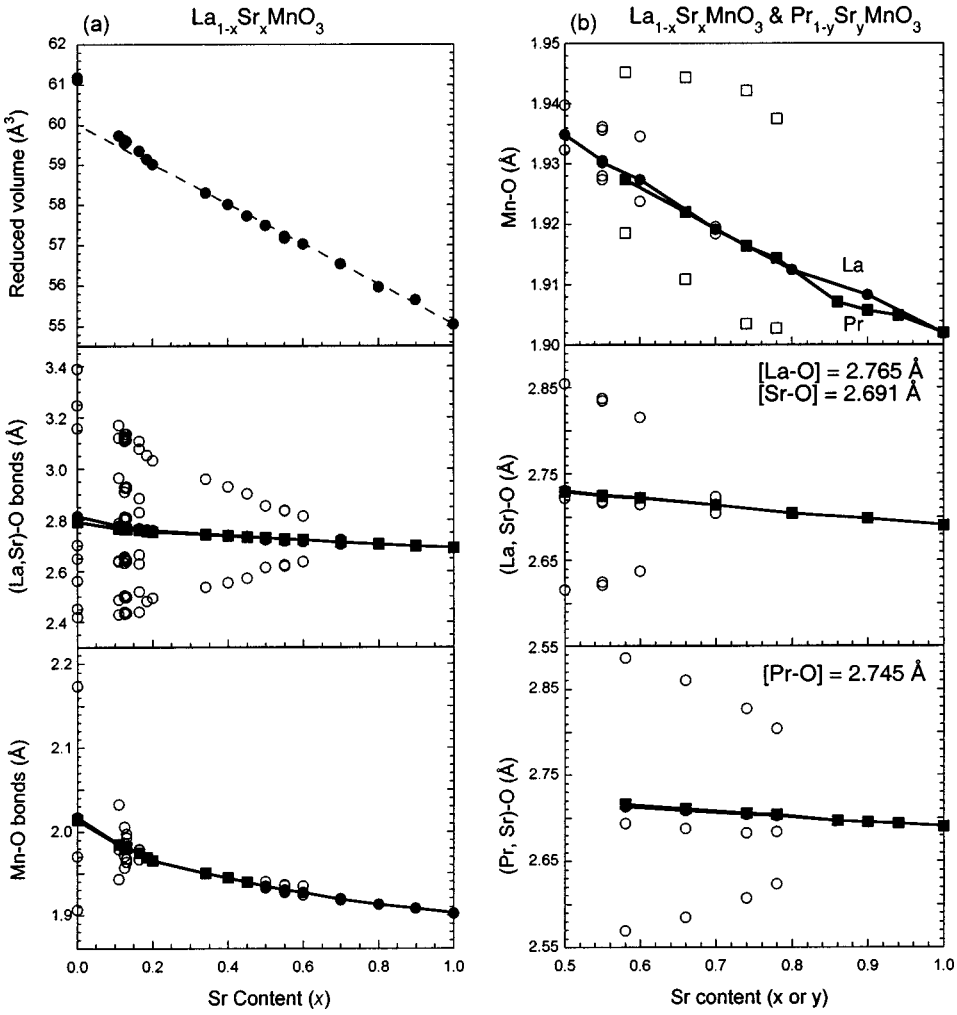

FIG. 7. (a) Room temperature reduced unit cell volume of the $La_{1-x}Sr_xMnO_3$ series showing the smooth and continuous decrease of the volume as a function of increasing x. Individual (open symbols) and average (solid lines) (La, Sr)-O and Mn-O bond lengths extracted from the $La_{1-x}Sr_xMnO_3$ series are also shown. (b) The Mn-O, [La, Sr]-O, and (Pr, Sr)-O bond lengths for both $La_{1-x}Sr_xMnO_3$ and $Pr_{1-y}Sr_yMnO_3$ series for Sr content x or $y \geqslant 0.5$ from which equilibrium [La-O], [Pr-O], and [Sr-O] interatomic distances were determined (see text for details).

are almost exactly the same. The decrease in the average Mn-O bond length with increasing x is consistent with the smaller ionic size of Mn^{4+} than that of Mn^{3+}. This decrease is controlled by the formal valence of Mn^{3+x} and not by the size of ions on the perovskite A site. On the other hand, we clearly observe different average bondlengths for (La, Sr)-O and (Pr, Sr)-O. From these bonds we have obtained the following equilibrium interatomic distances: [La-O] $=2.765(2)$ Å$>$[Pr-O]$=2.745(2)$ Å$>$[Sr-O]$=2.691(2)$ Å for twelve coordinated A-site ions. Obviously the ionic size of Sr is smaller than that of La and Pr in ''discord'' with the tabulated values in Shannon's tables[30] for nine or twelve coordinated ions.

For $La_{1-x}Sr_xMnO_3$ with $x>0.5$ and $Pr_{1-y}Sr_yMnO_3$ with $y>0.5$, AFM ordering of the Mn moments occurs for all studied compositions at some temperature below 300 K. As shown in Fig. 6, the magnetic ordering transitions coincide with structural transitions from cubic to tetragonal or from tetragonal to orthorhombic in some regions of the phase diagrams, but at compositions of roughly $0.6 \leqslant x \leqslant 0.8$ magnetic ordering occurs with the structures remaining tetragonal. Also at the highest substitution levels, roughly $0.95 \leqslant x \leqslant 1.0$, the structure remains cubic at low temperature. The magnetic structures are A, C, and G type, as shown in Fig. 6(b). The G-type configuration consists of Mn spins being aligned antiparallel to each other along the three directions. The C-type ordering is characterized by the AFM coupling of ferromagnetic Mn chains that point along the longest crystallographic axis of the unit cell [i.e., along the long Mn-O(1) bond which is the direction of the c axis; for $x=0.55$ at 225 K, the Mn spins are arranged ferromagnetically, consistent with the magnetic measurements, with a FM moment of $\sim 1.44 \mu_B$ and $2\times$Mn-O(1)~ 1.937 Å, $4\times$Mn-O(2) ~ 1.926 Å, and Mn-O(2)-Mn$\sim 170.25°$]. The A-type magnetic structure consists of antiferromagnetically coupled parallel ferromagnetic planes (sheets) that are perpendicular to the shortest axis of the unit cell with the Mn spins pointing along the longest axis (spins lie in the planes). The AFM coupling of the ferromagnetic planes takes place along the shortest axis, thus, leading to a short Mn-O(3) distance in this direction. As such, the Mn octahedron becomes distorted with four long Mn-O bonds [$2\times$Mn-O(1)~ 1.946 Å, $2\times$Mn-O(2)~ 1.940 Å for $x=0.55$ at 12 K] in the ferromagnetic planes and two short Mn-O(3) of ~ 1.899 Å bonds perpendicular to them. The Mn-O(2)-Mn and Mn-O(3)-Mn bond angles are 169.9° and 168.9°, respectively.

For $x=0.5$, 0.55, 0.6, $0.8 \leqslant x < 1$, $y=0.58$ and $0.78 \leqslant y < 1$, antiferromagnetic and nuclear structural transitions take

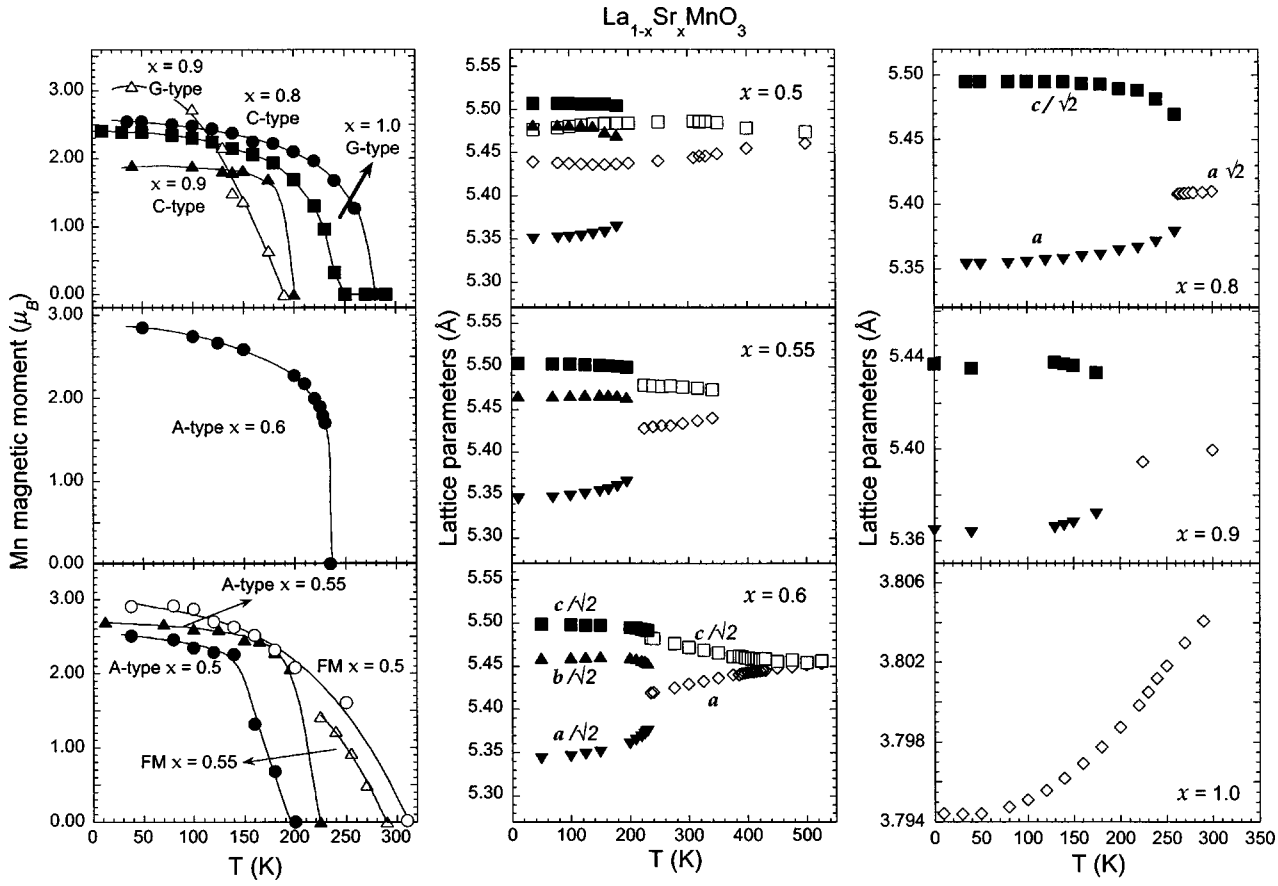

FIG. 8. (Left) refined Mn magnetic moment for $x=0.5$, 0.55, 0.6, 0.8, 0.9, and 1. For $x=0.9$, both the *C*- and *G*-type refined moments are plotted. The *C*-type Mn spins order suddenly as evidenced in the abrupt appearance of the magnetic peaks as the temperature is lowered. Ferromagnetic ($x=0.5$, 0.55; open circles) and *G*-type magnetic transitions ($x=1.0$) are not first-order. (Middle) lattice parameters of $x=0.5$, 0.55 and 0.6 as a function of temperature. For $x=0.5$, the figure shows lattice parameters for both the coexisting tetragonal and orthorhombic phases below T_N. (Right) lattice parameters for $x=0.8$, 0.9, and 1.0 as a function of temperature.

place at exactly the same temperature. These transitions are first order (except for $x=1.0$) as indicated by the abrupt discontinuity of the refined magnetic moment, lattice parameters (Figs. 8, 9), and the hysteretic behavior of the resistivity and magnetic susceptibility measured upon cooling and heating (Fig. 4). For $0.6 \leqslant x \leqslant 0.8$ and $0.58 < y \leqslant 0.78$, structural transitions precedes the magnetic transitions.

Among all samples, the $x=0.94$ and 0.95 samples are particularly interesting because they lie near or at the bottom of a valley on the phase diagram (within the resolution of our compositional grid) that separates the *C*- and *G*-type antiferromagnetic states by a sharp nearly ''vertical'' boundary line (see Fig. 6). $La_{0.05}Sr_{0.95}MnO_3$ has the lowest T_N value of $\sim$104 K when compared to its neighbors (for example, $\sim$240 K for $SrMnO_3$, and $\sim$140 and 200 K for $x=0.94$ and 0.9, respectively). Neutron diffraction data for $La_{0.06}Sr_{0.94}MnO_3$—displayed in Fig. 10—show a single phase cubic 200 reflection in the *d*-spacing range of 1.8–2 Å above 140 K and a partial transformation to the tetragonal $I4/mcm$ structure (220 and 004 reflections) at lower temperatures. For these $x=0.9-0.95$ samples, a strong competition between the AFM *C*- and *G*-type states appears to be taking place resulting in a phase separation and the coexistence of the two states at low temperatures. Figure 11, shows portions of raw neutron diffraction data in the *d*-spacing range of 3 to 6 Å for $x=0.8$, 0.9 and 1.0. As shown in the figure, magnetic peaks of the *C* type appear below 263 K in the $x=0.8$ neutron diffraction patterns, of the *G* type below 240 K in the $x=1.0$ patterns, and of *C* and *G* types below 200 and $\sim$155 K, respectively, for $x=0.9$. It is worth noting that the most favorable agreement factors of our refinements were obtained when the tetragonal and cubic structures were associated with the *C*- and *G*-type magnetic states, respectively, and that the weight fraction of the *G*-type phase refined to $\sim$14 and 30 % for $x=0.9$ and $x=0.94$, respectively. This observed phase coexistence (separation) is in agreement with several theoretical models[31–35] suggesting that unstable canted antiferromagnetic structures result in electronic phase separation into different magnetic domains (FM-AFM domains or AFM-AFM domains). Yunoki *et al.*[34,35] suggested that this tendency to phase separation seems to be an intrinsic property of the double exchange model. Recent neutron scattering[36–38] and NMR (Ref. 39) measurements gave an experimental evidence for the existence of such a phase separation in $La_{1-x}Ca_xMnO_3$ with $0.92 < x < 0.97$, for example,[38] in the form of ferromagnetic droplets within the host AFM structure. We should note, however, that such a FM phase is not observed in the $La(Pr)_{1-x}Sr_xMnO_3$ systems

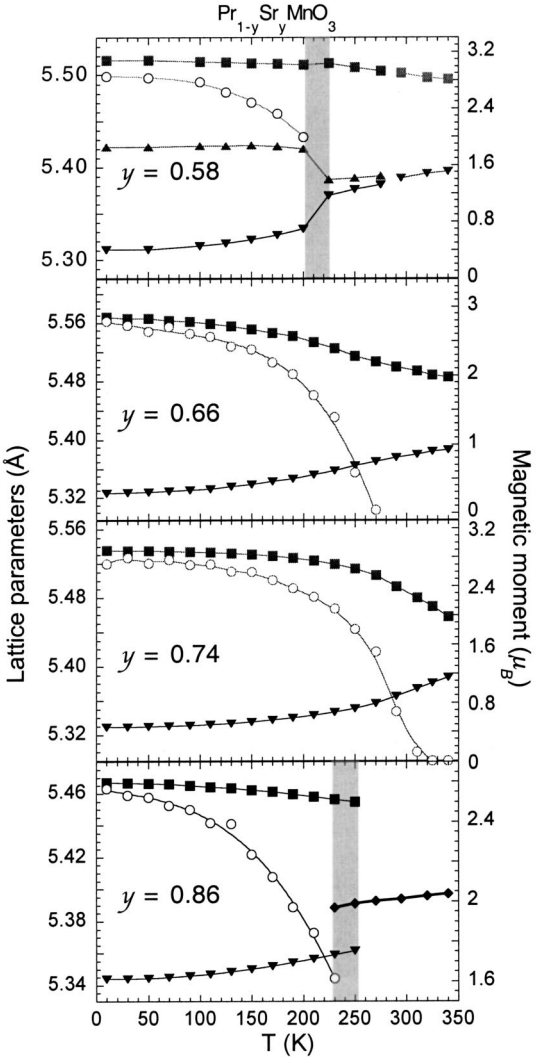

FIG. 9. Lattice parameters (filled symbols) and refined magnetic moments (open symbols) of $Pr_{1-y}Sr_yMnO_3$ ($y=0.58$, 0.66, 0.74, and 0.86).

at the cubic (*G*-type)/tetragonal (*C*-type) phase boundary but as will be seen in the next paragraph phase separation of FM-AFM domains does occur for $x=0.5$.

For $La_{0.5}Sr_{0.5}MnO_3$, charge and/or orbital ordering of the Mn^{3+} and Mn^{4+} ions could be expected in a way similar to what was observed in $La_{0.5}Ca_{0.5}MnO_3$ (Ref. 40) and $Nd_{0.5}Ca_{0.5}MnO_3$,[41] for example. We, therefore, examined the structural behavior of $La_{0.5}Sr_{0.5}MnO_3$ at temperatures between 38 and 450 K and found that it crystallizes in a tetragonal structure of space group $I4/mcm$ between 135 and 450 K (approaching cubic symmetry at 450 K). As for the magnetic structure, the Mn spins first align ferromagnetically at temperatures below 320 K and then antiferromagnetically at temperatures below 135 K (T_N). Below T_N, part of the sample gradually transforms from the FM tetragonal $I4/mcm$ phase to an orbital-ordered *A*-type AFM orthorhombic *Fmmm* phase and the two phases coexist at our lowest measured temperature of 38 K. Our data could not provide any evidence for charge ordering in this $La_{0.5}Sr_{0.5}MnO_3$ phase.

The quality of our $La_{0.5}Sr_{0.5}MnO_3$ sample as a single-

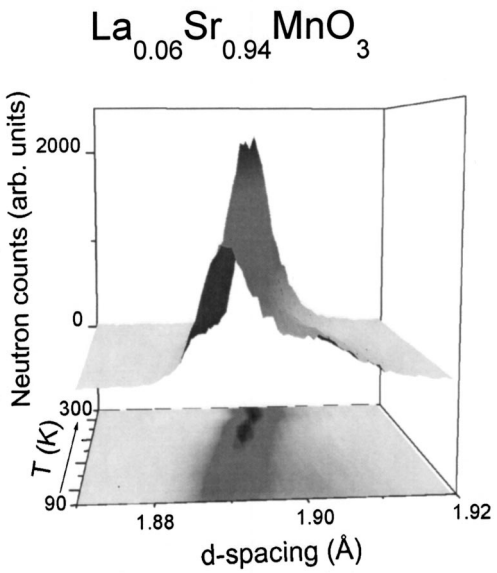

FIG. 10. Splitting of the cubic 200 reflection ($La_{0.06}Sr_{0.94}MnO_3$ sample) into two tetragonal 220 and 004 reflections as a function of decreasing temperature.

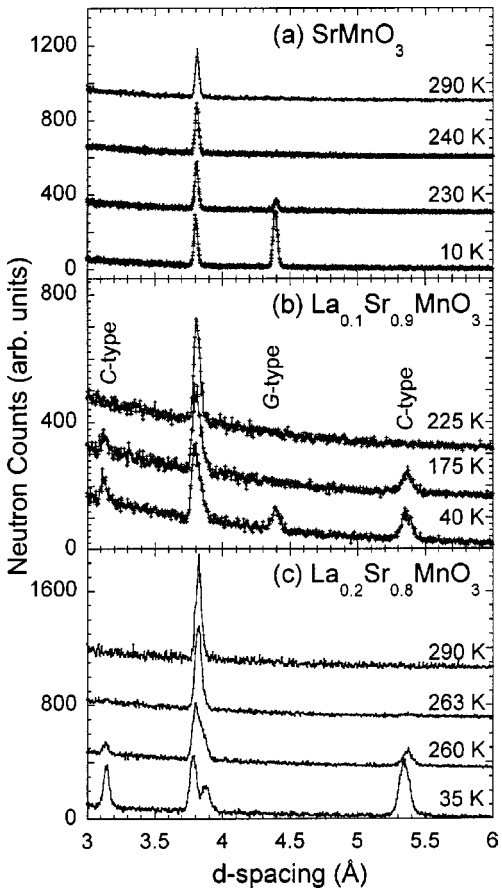

FIG. 11. Raw neutron diffraction data in the *d*-spacing range of 3 to 6 Å showing magnetic peaks of the *C*-type for $x=0.8$, of the *G*-type for $x=1.0$ and of the *C*- and *G*-types for $x=0.9$ (see text for more details).

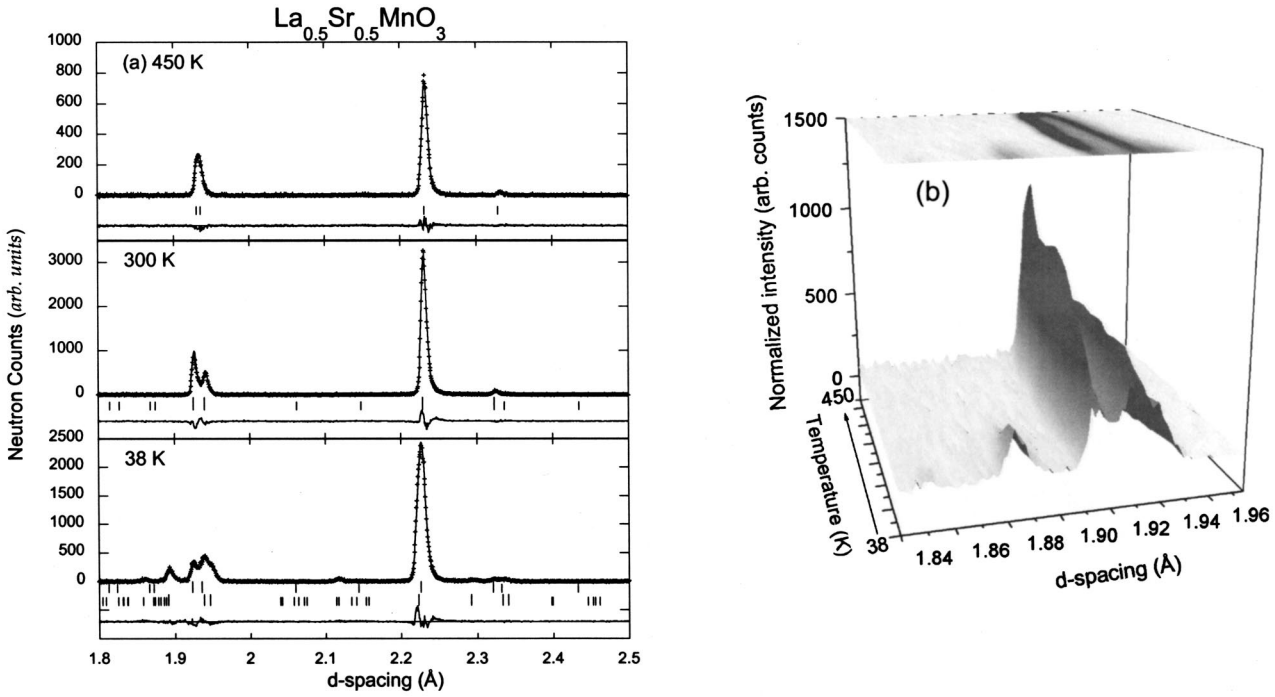

FIG. 12. (a) Best fit Rietveld refinements for $La_{0.5}Sr_{0.5}MnO_3$ at 38, 300, and 450 K showing a pseudocubic tetragonal single phase material near 450 K, a tetragonal $I4/mcm$ structure between 150 (T_N) and 450 K, and the coexistence of tetragonal and orthorhombic phases below T_N. (b) Splitting of the tetragonal 220 and 004 peaks into orthorhombic peaks below 150 K for $La_{0.5}Sr_{0.5}MnO_3$.

phase material at all temperatures above 135 K and the evolution of the tetragonal 220 and 004 peaks as a function of decreasing temperature are shown in Figs. 12(a) and 12(b), respectively. The coexistence, at 38 K, of ~44% (by weight) of the FM tetragonal phase with 56% of the AFM orthorhombic phase is an indication of a strong competition between these two magnetic states—in agreement with van der Brink and Khomskii's calculations[5] that predict very similar energies for the FM and the *A*- and *C*-type AFM states—that end up in a phase separation, Fig. 8(a). The exact nature and shape of this phase separation need to be investigated by direct analytical techniques such as HRTEM, for example. However, there are at least two models that may explain our results: model (a), phase separation taking place at the microscopic level within each grain which means that the orthorhombic phase starts nucleating within the tetragonal matrix (grain) and then, as the temperature is lowered, the grain size of the orthorhombic phase increases at the expense of the grain size of the host matrix and model (b), some of the tetragonal grains convert wholly to the orthorhombic phase while the remaining grains would remain tetragonal. In either of these two models, one would expect the development of considerable strains below the phase transition whether due to the two phases coexisting within the same grain or in proximity of each other. On the other hand, the grain size of the two phases is expected to vary in model (a) and to remain constant in model (b). As such, the analysis of the peak broadening and peak shape parameters as a function of temperature may weigh in favor of one of the two models. Our refinements were carried out including four independent sets of peak shape parameters (for the nuclear and magnetic phases). On the other hand, an isotropic peak broadening model was assumed because of the resolution limit of our data and the overlap of many peaks of the different phases. As shown in Fig. 13(a), a considerable strain of up to ~0.4% develops below the tetragonal to orthorhombic structural phase transition temperature. The magnitude of these strains is similar to those obtained in brominated $YBa_2Cu_3O_{6+\delta}$ for which the nuclear Bragg peaks were severely broadened.[42] The grain size of the tetragonal phase appears to be constant at temperatures above ~220 K but then decreases continuously as the temperature is lowered below ~220 K, Fig. 13(b). An opposite behavior is observed, as expected, for the grain size of the orthorhombic phase which increases below the temperature of structural phase transition. The grain size of the AFM domains is, on the other hand, smaller than that of the nuclear phase and appears to be constant at about 750 Å as shown in Fig. 13(b). Because of the overlap of the magnetic and nuclear peaks for the FM tetragonal phase, the calculated FM domains were similar in size to the corresponding nuclear tetragonal phase but with much larger error bars (not shown). We should note, however, that the large error bars for the values of the grain size of the orthorhombic phase are due to the fact that this phase grows from a few percent (by weight) at 180 K up to a maximum of 56% at 38 K. Thus, our results suggest that phase separation in $La_{0.5}Sr_{0.5}MnO_3$ takes place according to model (a) which is also in agreement with the TEM observations of Uehara's *et al.*[43] of coexisting sub-micrometer size magnetic and nuclear domains within the same grain in $La_{0.5}Ca_{0.5}MnO_3$. Furthermore, Huang *et al.*,[44] reported a neutron diffraction study showing the existence of a similar phase separation in $La_{0.5}Ca_{0.5}MnO_3$ and at the onset of the phase separation they

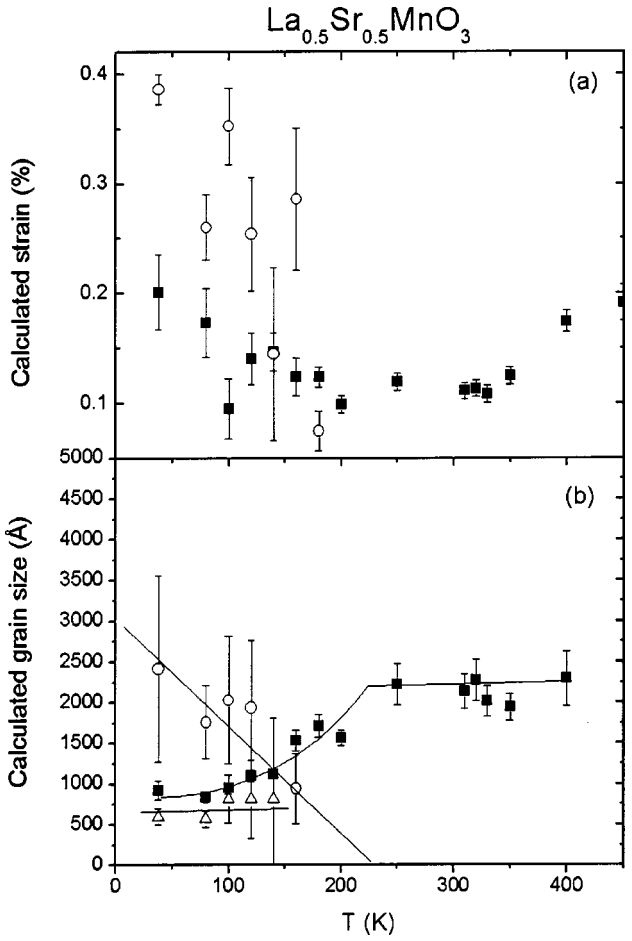

FIG. 13. $La_{0.5}Sr_{0.5}MnO_3$: Calculated strains (a) and grain size (b) for the tetragonal phase (filled symbols) and orthorhombic phase (open circles). The grain size of the AFM domains is represented by open triangles.

observed Bragg peaks that were at least three times as broad as their instrument resolution. The existence of phase separation in other CMR manganites was also reported by other groups.[43–46] Also shown in Fig. 13(b), the behavior of the grain size for both the tetragonal and orthorhombic phases can be extrapolated to about 220 K suggesting that the nucleation of the orthorhombic phase may have started at this temperature but that this phase grows to reach a sufficient coherence length for neutron diffraction peaks to be observed only below ~180 K.

Based on the above observations, we expect interesting features in the resistivity and magnetization measurements for this $x=0.5$ sample. Indeed, resistivity measurements show a metallic behavior for the sample at all temperatures up to 400 K with a kink at ~320 K that corresponds to the ferromagnetic ordering of the Mn spins. Below 180 K, however, no increase in resistivity was observed that would otherwise be in agreement with the observed antiferromagnetic ordering of the sample. The sample remained metallic to the lowest temperatures of our measurements. It is important to note, however, that the two dimensional ferromagnetic sheets may still be conducting and that a large fraction of the tetragonal *metallic* FM phase remained present to the lowest temperatures thus providing an easy path for conductivity. These results are in good agreement with the results of Akimoto *et al.*[16] and Moritomo *et al.*[17] showing a metallic behavior for their *A*-type AFM $La_{0.5}Sr_{0.5}MnO_3$ and $La_{0.46}Sr_{0.54}MnO_3$ samples, respectively. The samples studied in these references, however, also contain a fair amount of FM metallic tetragonal and/or rhombohedral phases at the lowest temperatures.

To better understand the metallic behavior of our $x=0.5$ sample, it became necessary to investigate other compositions for x near 0.5 that exhibit less competition between the FM and AFM states (i.e., for compositions in which all the sample transforms suddenly from tetragonal to orthorhombic over a very narrow temperature range). The $x=0.55$ and $x=0.6$ samples provide this opportunity. As shown in Fig. 6, the $x=0.55$ sample undergoes a series of transitions: paramagnetic (PM) tetragonal to FM tetragonal and then a sudden structural and magnetic phase transition to an AFM orthorhombic single phase below ~200 K. The $x=0.6$ sample shows a direct transition from the PM tetragonal phase to the AFM orthorhombic phase without ever becoming ferromagnetic (within the resolution of our measurements), Fig. 14. Lattice parameters for the $x=0.5$, 0.55, 0.6 samples displayed in Fig. 8 show the first-order nature of the structural transition from the tetragonal phase to the orthorhombic phase. Once again, the hysteretic behavior of the resistivity and magnetic susceptibility confirm that this structural transition is first order. For $x=0.55$, resistivity measurements also show a semiconductinglike behavior in the paramagnetic region, a metallic behavior when the material becomes FM and an insulating behavior in the AFM region. The $x=0.60$ sample is insulating at all temperatures with a very weak kink in the resistivity observed at T_N. These results clearly show that a metallic behavior of our ceramic samples is observed only when the sample is ferromagnetic or when it contains a fraction of a ferromagnetic phase. However, our resistivity measurements should not be considered conclusive because of the ceramic nature of the samples and the presence of grain boundaries. Thus, our data cannot conclusively rule out the metallic behavior of the *A*-type AFM materials. Indeed, it is possible that the ground state of the *A*-type AFM configuration may be metallic due to its 2D character and to the metallic property of the ferromagnetic sheets but then one would expect a strong anisotropy in the electrical and transport properties between the directions that are parallel or perpendicular to these ferromagnetic sheets. Suggestions of such a behavior have actually been proposed in the literature but to the best of our knowledge, no conclusive proof has been so far presented. Obviously, to prove this point various measurements on a single crystal should be conducted along the different directions of the crystal. In agreement with this argument, Kawano *et al.*,[47] using inelastic neutron scattering, showed that spin waves propagating within the ferromagnetic planes have the greatest spin wave energy and that the spin wave dispersion relations, for the *A*-type antiferromagnetic $Nd_{0.45}Sr_{0.55}MnO_3$, are anisotropic as determined from the excitation measurements along the directions parallel and perpendicular to the ferromagnetic planes.

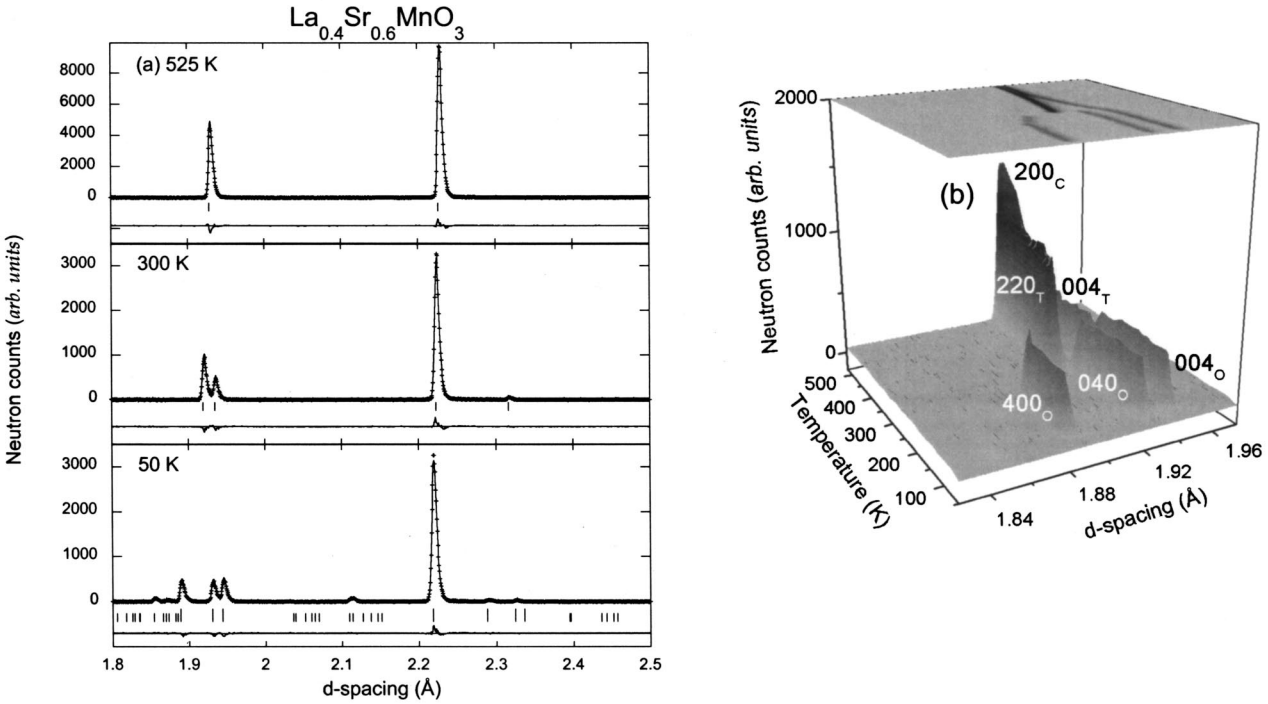

FIG. 14. (a) Best fit Rietveld refinements for $La_{0.4}Sr_{0.6}MnO_3$ at 50, 300, and 525 K showing cubic, tetragonal, and orthorhombic structures, respectively. (b) Evolution of the Bragg peaks between 1.8 and 2 Å as a function of temperature.

CONCLUSIONS

$La_{1-x}Sr_xMnO_3$ samples with $0.5 \leqslant x \leqslant 1$ were synthesized and studied in a single-phase stoichiometric perovskite form. $Pr_{1-y}Sr_yMnO_3$ samples covering the composition range $0.58 \leqslant y \leqslant 1$ were also synthesized. We investigated the magnetic and resistive properties and the structural behavior of these compounds as a function of temperature. Our results enabled the construction of the full structural and magnetic phase diagram for $La_{1-x}Sr_xMnO_3$ and a partial phase diagram for highly doped $Pr_{1-y}Sr_yMnO_3$. We show that there is a strong competition between ferromagnetism and antiferromagnetism for $x \sim 0.5$ and a similar competition between *C*-type and *G*-type AFM for $x \sim 0.95$. It is interesting to note that for x or $y \sim 0.95$-where the Mn-O-Mn bond angles are only slightly distorted-we do not observe any intermediate FM phase similar to that observed in $(R, Ca)MnO_3$ systems that have considerably larger Mn-O-Mn distortions. It is also important to note that the magnetic transitions are coupled with first-order structural transitions for $0.8 \leqslant x \leqslant 0.95$ and $0.8 \leqslant y \leqslant 0.95$. For other compositions in which the structural and magnetic transitions occur independently at different temperatures, the structural phase transitions are of second order. Examining the various AFM configurations, we find that the *A*-type magnetic structure is favored when the MnO_6 octahedra possess two short Mn-O and four long bond lengths, thus, giving rise to orthorhombic *Fmmm* symmetry and to AFM interactions along the short bonds. On the other hand, the *C*-type magnetic phase is characterized by two long Mn-O bond lengths along which the ferromagnetic interactions take place and four short Mn-O bonds and the host structure is tetragonal. Finally, we used our data to find the equilibrium interatomic distances for [La-O], [Pr-O], and [Sr-O]. Contrary to the common expectation, [Sr-O] is actually shorter than the interatomic distances of [La-O] or [Pr-O]. The use of correct interatomic distances is important for the calculation of tolerance factors and for the prediction of stability and properties of perovskite magnitudes.[29]

ACKNOWLEDGMENTS

Work at NIU was supported by the DARPA/ONR, Grant No. NSF-DMR-0105398, and by the State of Illinois under HECA. At ANL, this work was also supported by the U.S. Department of Energy, Division of Basic Energy Science-Materials Sciences, under Contract No. W-31-109-ENG-38 (the operation of IPNS).

[1] Z. Fang, I. V. Solovyev, K. Terakura, Phys. Rev. Lett. **84**, 3169 (2000).

[2] A. Maignan, C. Martin, F. Damay, B. Raveau, and J. Hejtmanek, Phys. Rev. B **58**, 2758 (1998).

[3] J. Hejtmanek, Z. Jirak, M. Marysko, C. Martin, A. Maignan, M. Hervieu, and B. Raveau, Phys. Rev. B **60**, 14 057 (1999).

[4] Y. Konishi, Z. Fang, M. Izumi, T. Manako, M. Kasai, H. Kuwahara, M. Kawasaki, K. Terakura, and Y. Tokura,

J. Phys. Soc. Jpn. **68**, 3790 (1999).
[5] J. van der Brink and D. Khomskii, Phys. Rev. Lett. **82**, 1016 (1999).
[6] B. Dabrowski, X. Xiong, Z. Bukowski, R. Dybzinski, P. W. Klamut, J. E. Siewenie, O. Chmaissem, J. Shaffer, and C. W. Kimball, Phys. Rev. B **60**, 7006 (1999).
[7] H. Kawano, R. Kajimoto, M. Kubota, and H. Yoshizawa, Phys. Rev. B **53**, R14 709 (1996).
[8] M. C. Martin, G. Shirane, Y. Endoh, K. Hirota, Y. Moritomo, and Y. Tokura, Phys. Rev. B **53**, 14 285 (1996).
[9] J. F. Mitchell, D. N. Argyriou, C. D. Potter, D. G. Hinks, J. D. Jorgensen, and S. D. Bader, Phys. Rev. B **54**, 6172 (1996).
[10] C. Martin, A. Maignan, M. Hervieu, B. Raveau, Z. Jirak, A. Kurbakov, V. Trounov, G. Andre, and F. Bouree, J. Magn. Magn. Mater. **205**, 184 (1999).
[11] C. Martin, A. Maignan, M. Hervieu, and B. Raveau, Phys. Rev. B **60**, 12 191 (1999).
[12] F. Damay, C. Martin, M. Hervieu, A. Maignan, B. Raveau, G. André, and F. Bourée, J. Magn. Magn. Mater. **184**, 71 (1998).
[13] K. Kikuchi, H. Chiba, M. Kikuchi, and Y. Syono, J. Solid State Chem. **146**, 1 (1999).
[14] S. L. Yuan, Y. Jiang, X. Y. Zeng, W. Y. Zhao, Y. P. Yang, J. P. Qian, G. Q. Zhang, F. Tu, and C. Q. Tang, Phys. Rev. B **62**, 11 347 (2000).
[15] L. Rormark, K. Wiik, S. Stolen, and T. Grande, J. Mater. Chem. **12**, 1058 (2002).
[16] T. Akimoto, Y. Maruyama, Y. Moritomo, A. Nakamura, K. Hirota, K. Ohoyama, and M. Ohashi, Phys. Rev. B **57**, R5594 (1998).
[17] Y. Moritomo, T. Akimoto, A. Nakamura, K. Ohoyama, and M. Ohashi, Phys. Rev. B **58**, 5544 (1998).
[18] Z. Jirak, J. Hejtmanek, K. Knizek, M. Marysko, V. Sima, and R. Sonntag, J. Magn. Magn. Mater. **217**, 113 (2000).
[19] J. Hejtmanek, Z. Jirak, E. Pollert, D. Sedmidubsky, A. Strejc, C. Martin, A. Maignan, and V. Hardy, J. Appl. Phys. **91**, 8275 (2002).
[20] K. Knízek, Z. Jirák, E. Pollert, F. Zounová, and S. Vratislav, J. Solid State Chem. **100**, 292 (1992).
[21] D. N. Argyriou, D. G. Hinks, J. F. Mitchell, C. D. Potter, A. J. Schultz, D. M. Young, J. D. Jorgensen, and S. D. Bader, J. Solid State Chem. **124**, 381 (1996).
[22] H. Kawano, R. Kajimoto, H. Yoshizawa, Y. Tomioka, H. Kuwahara, and Y. Tokura, Phys. Rev. Lett. **78**, 4253 (1997).
[23] A. Llobet, J. L. García-Munoz, C. Frontera, and C. Ritter, Phys. Rev. B **60**, R9889 (1999).
[24] D. G. Hinks, B. Dabrowski, J. D. Jorgensen, A. W. Mitchell, D. R. Richards, and D.-L. Shi, Nature (London) **333**, 836 (1988).
[25] J. D. Jorgensen, J. J. Faber, J. M. Carpenter, R. K. Crawford, J. R. Haumann, R. L. Hitterman, R. Kleb, G. E. Ostrowski, F. J. Rotella, and T. G. Worton, J. Appl. Crystallogr. **22**, 321 (1989).
[26] A. C. Larson and R. B. von Dreele, General Structure Analysis System GSAS, University of California, 1985–1990.
[27] Q. Huang, A. Santoro, J. W. Lynn, R. W. Erwin, J. A. Borchers, J. L. Peng, and R. L. Greene, Phys. Rev. B **55**, 14 987 (1997).
[28] X. Xiong, B. Dabrowski, O. Chmaissem, Z. Bukowski, S. Kolesnik, R. Dybzinski, and J. D. Jorgensen, Phys. Rev. B **60**, 10 186 (1999).
[29] B. Dabrowski, O. Chmaissem, J. Mais, S. Kolesnik, J. D. Jorgensen, and S. Short, J. Solid State Chem. **170**, 154 (2003).
[30] R. D. Shannon, Acta Crystallogr., Sect. A: Found. Crystallogr. **32**, 751 (1998).
[31] E. L. Nagaev, Sov. Phys. Usp. **39**, 781 (1996).
[32] E. L. Nagaev, Phys. Rev. B **58**, 2415 (1998).
[33] L. P. Gor'kov, Sov. Phys. Usp. **41**, 589 (1998).
[34] S. Yunoki, J. Hu, A. L. Malvezzi, A. Moreo, N. Furukawa, and E. Dagatto, Phys. Rev. Lett. **80**, 845 (1998).
[35] S. Yunoki, A. Moreo, and E. Dagatto, Phys. Rev. Lett. **81**, 5612 (1998).
[36] M. Hennion, F. Moussa, J. Rodriguez-Carvajal, L. Pinsard, and A. Revcholevski, Phys. Rev. Lett. **81**, 1957 (1998).
[37] M. Hennion, F. Moussa, G. Biotteau, J. Rodriguez-Carvajal, L. Pinsard, and A. Revcholevski, Phys. Rev. B **61**, 9513 (2000).
[38] J. J. Neumeier and J. L. Cohn, Phys. Rev. B **61**, 14 319 (2000), and references therein.
[39] G. Allodi, R. de Renzi, G. Guidi, F. Licci, and M. W. Pieper, Phys. Rev. B **56**, 6036 (1997); G. Allodi, R. de Renzi, and G. Guidi, *ibid.* **57**, 1024 (1998).
[40] P. G. Radaelli, D. E. Cox, M. Marezio, and S.-W. Cheong, Phys. Rev. B **55**, 3015 (1997).
[41] F. Millange, S. de Brion, and G. Chouteau, Phys. Rev. B **62**, 5619 (2000).
[42] D. G. Hinks, O. Chmaissem, L. Ely, C. Scott, J. D. Jorgensen, and J. K. Akujieze, Physica C **333**, 1 (2000), and references therein.
[43] M. Uehara, S. Mori, C. H. Chen, and S.-W. Cheong, Nature (London) **399**, 560 (1999).
[44] Q. Huang, J. W. Lynn, R. W. Erwin, A. Santoro, D. C. Dender, V. N. Smolyaninova, K. Ghosh, and R. L. Greene, Phys. Rev. B **61**, 8895 (2000).
[45] M. M. Savosta, V. A. Borodin, M. Marysko, Z. Jirak, J. Hejtmanek, and P. Novak, Phys. Rev. B **65**, 224418 (2002).
[46] S. I. Patil, S. M. Bhagat, Q. Q. Shu, S. E. Lofland, S. B. Ogale, V. N. Smolyaninova, X. Zhang, B. S. Palmer, R. S. Decca, F. A. Brown, H. D. Drew, R. L. Greene, I. O. Troyanchuk, and W. H. McCarroll, Phys. Rev. B **62**, 9548 (2000).
[47] H. Kawano, R. Kajimoto, H. Yoshizawa, J. A. Fernandez-Baca, Y. Tomioka, H. Kuwahara, and Y. Tokura, Physica B **241**, 289 (1998).